K-Space Aware Multi-Static Millimeter-Wave Imaging

Mahmoud Kazemi , Zahra Kavehvash , and Mahdi Shabany , *Member, IEEE*

Abstract—**This paper focuses on an efficient approach for designing multi-static arrays for millimeter-wave imaging, based on the *k*-space or Fourier-spatial domain characteristic of imaging systems. Our goal is to decrease the redundancy of the data measured by each antenna and to improve the resolution of the reconstructed image. The proposed technique is based on determining the role of each transmitter and receiver, in collecting the data from each voxel of the target in *k*-space domain and then rotating the transmitters' beams to measure the desirable information. The effect of non-uniform redundant *k*-space domain frequency samples that act as an undesirable filter is compensated using a modified SAR back-projection algorithm. The experimental and simulation results are presented and compared with that of a sparse multi-static array with the same number of transmitters and receivers. Our simulations and measurements show significant improvement in terms of overall quality and edge preservation in the reconstructed images. Also, the obtained results demonstrate that using the proposed structure and algorithm, the average improvement in peak-signal-to-noise ratio, structural similarity index measure, and digital image correlation metrics of 3.03, 0.22, and 0.173 dB, respectively, are acheived.**

Index Terms—**Millimeter-wave imaging, multi-static arrays, spatial Fourier domain, image reconstruction, super resolution.**

I. INTRODUCTION

RECENTLY millimeter-wave imaging has been used in various applications, such as security surveillance, medical imaging and civil structures inspection. As the threat from terrorist attacks is growing, novel ways to enhance security inspection systems at checkpoints are in demand. Millimeter-wave imaging not only is an effective option of penetrating into dielectric materials including cloth, but also provides suitable imaging resolution [1], [2]. Moreover, millimeter-wave imaging is capable of identifying different materials [3], which makes it a promising option for concealed weapon detection [1]. The non-ionizing characteristic of millimeter-waves is used in non-invasive imaging for breast [4] and skin cancer [5] detection, as an alternative to more harmful systems based on X-Ray illumination. Millimeter wave imaging is also used in civil structures inspection as described in [6] to spot cracks under wallpaper.

Most commercially available imaging devices, are designed based on mono-static structures [1], [7]. Such structures

are subject to some artifacts appeared in the reconstructed image, where multiple reflections of wave cause unreal lines in the output image [8]. So, multi-static and bi-static structures [9], [10], in which multiple angular viewing of the object allows enhancing the imaging result, can be considered as an alternative for mono-static imaging.

The high cost and large computational complexity are two main challenges of multi-static structures. The issue of large computational complexity has been addressed in many works through proposing different FFT-based algorithms [8], [11]–[13]. On the other side, the cost reduction in multi static systems has been approached through designing different sparse arrays [14]–[16]. In [14], the receiver array in a single transmitter structure, is sub-sampled. However, sub-sampling of antennas to address the high cost of multi-static structures, degrades the imaging quality. Moreover, in [14], it is stated that, subsampling causes off-centered objects to lose some part of their frequency spectrum. This loss was compensated by replicating the frequency spectrum and band-pass filtering the result. But, this process is simply equivalent to a sequence of shifting in frequency domain, which is inherent in the SAR back-projection (SAR-BP) algorithm, and then low-pass filtering. Furthermore, this is based on the assumption that, like the mono-static structures, the detected spectral bandwidth of the object is narrow enough, allowing to subsample without causing aliasing. Still, as will be shown in Section II, the measured spectral span of the object in a multi-static structure is different and wider than that of its mono-static counterpart. Subsampling without considering this spectral span, resulted in an aliased data in that paper, in spite of their expectations.

In [15], a method to design sparse multi-static arrays based on the effective aperture concept in ultrasonic imaging [17], is introduced. In this method, an approximated equivalent mono-static aperture based on the convolution of transmitter and receiver arrays is determined, to compare the performance of different panel-based multi-static antenna arrangements. Still, the proposed sparse arrays based on the concept of effective aperture, although fully sample the spatial domain based on the Nyquist criteria, do not guarantee full sampling of the frequency domain, which in turn affects the overall resolution. In an attempt to address this problem, in [18], multi-static arrays are studied in k-space domain. In that paper, it is shown that multi-static arrays collect different redundant frequency samples from different voxels in the imaging aperture, while some frequency components are not captured from some voxels. The proposed reconstruction algorithm in [18], compensates such non-uniformities and results in a uniform recovered image with sharper edges. In this paper, we make

a connection between the effective aperture concept and the k-space analysis proposed in [18] and show that although the effective aperture concept is a low complexity approach to start with [15], the k-space analysis is a more sophisticated tool allowing to study and expand the measured frequency-terms of imaging voxels to improve the recovered image's resolution.

In another attempt to reduce the cost of multi-static systems, a 3D placement of transmitters is presented in [19], to achieve wider viewing angle, while keeping the receivers aperture small enough such that the overall cost of the multi-transmitter multi-static structure is reduced. In that paper, transmitters are placed off the receivers' panel, widening the viewing angle of the object. This allows to alleviate the problem of panel based structures to screen sides of 3D objects like the human body. The use of power detectors as receivers and the limited number of transmitters, has decreased the overall cost of the system and its computational complexity. Angular diversity is also utilized in a type of SAR imaging called spotlight mode. In this mode the radar beam is steered to keep the target within the illumination beam in a longer time. This widens the imaging aperture and improves the imaging resolution, at the expense of less spatial coverage [20]. Angular diversity of multi-static systems has also been studied and utilized in a quasi mono-static cylindrical structure [21], where the back-scattered signal of three transmitters radiating the object simultaneously, is captured with one receiver. This structure is indeed a conventional multi-static system, which helps in increasing the effective numerical aperture and thus resolution. Still, like other multi-static structures, no analysis on the captured spatial frequency content based on k-space vectors is performed for efficient capturing the spatial spectrum of object.

Our contribution in this paper is to define the role of each transmitter-receiver pair in determining the measured spectral data in a multi-static structure. Based on this analysis, we rotate the transmitters' beam in order to measure desirable frequency-terms. The difference between this approach that is presented for multi-static arrays, and the SAR spotlight mode of bi-static and mono-static imaging is that we don't keep steering the beam. Instead, based on the k-space analysis, we focus each transmitter's beam to a specific region of the imaging aperture. This method, not only enhances the resolution of the reconstructed image, but also reduces the redundancy and alleviates the non-uniformity in the measured spectral data. We also study the high computational cost of redundancy compensation in [18] and present a solution to alleviate it.

The paper is organized as follows. Section II outlines the concept of the k-space domain. In Section III, we introduce the k-space aware SAR back-projection (KA-SAR-BP) algorithm. In Section IV, the effective aperture concept and its relation to k-space analysis is discussed. The proposed imaging structure is presented in Section V. Section VI is devoted to highlight the simulations and experimental results. Finally, Section VII concludes the paper.

II. K-SPACE REPRESENTATION

In this section, the k-space representation of millimeter-wave imaging systems is briefly described (see [11], [15],
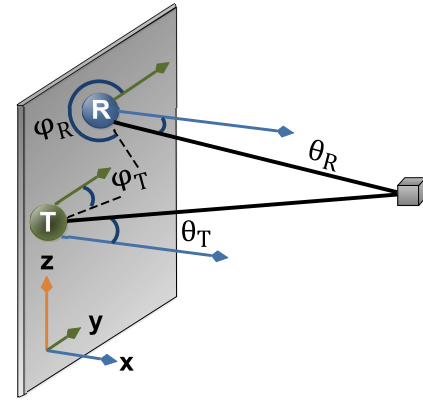

Fig. 1. A general millimeter-wave imaging system and a voxel in the space (R and T represent the location of a reciever and transmitter, respectively).
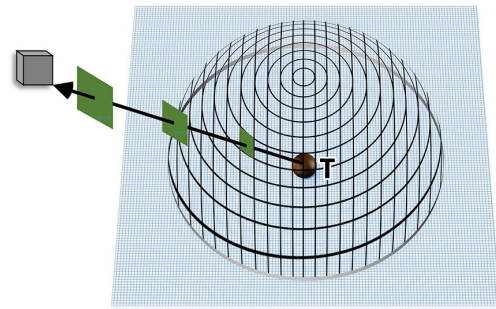

Fig. 2. Decomposition of spherical waves into superposition of plane wave components.

and [22] for details). As shown in Fig. 1, consider a general voxel in the space, illuminated by a point source transmitter, and the scattered field is measured by a single receiver. The Hankel's spherical function of the first kind, zeroth order [23], [24] emanating from antennas, is defined as:

$$E(\vec{r}, f) = \frac{e^{-jk|\vec{r}|}}{|\vec{r}|}, \tag{1}$$

where k denotes the wave number of the field, which is a frequency-dependent term in this and all following equations, $\vec{r}$ is the position vector and the origin is placed at transmitter's position. If we decompose this spherical-wave into superposition of plane-wave components, suppress the amplitude functions and constants and additional terms as shown in [1] and [24], we obtain:

$$E(\vec{r}, f) = \frac{e^{-jk|\vec{r}|}}{|\vec{r}|} \approx \int \int e^{-jk_x \text{x} - jk_y \text{y} - jk_z z} dk_z dk_y$$
$$= \int \int e^{-jk\hat{r}.\vec{r}} dk_z dk_y, \tag{2}$$

where $\hat{r}$ is the unit vector along $\vec{r}$. Figure 2 shows that only the plane-wave component along the vector connecting the transmitter to the given voxel will be scattered. In the same way, only the one along the vector from the voxel to the receiver will be measured, that allows us to omit the integration over k_y and k_z in (2). So the measured back-scattered field by

the receiver will be:

$$
\begin{aligned}
&E_{scatt}(z_R, y_R, z_T, y_T, f) \\
&= \int_{z_{vox,1}}^{z_{vox,2}} \int_{y_{vox,1}}^{y_{vox,2}} \int_{x_{vox,1}}^{x_{vox,2}} \rho(x,y,z) e^{-jk\hat{r}'.\vec{r}'} e^{-jk\hat{r}''.\vec{r}''} dx dy dz,
\end{aligned}
\tag{3}
$$

where $\rho(x,y,z)$ is the reflectivity function of the voxel, $z_{vox,1}, z_{vox,2}, y_{vox,1}, y_{vox,2}, x_{vox,1}, x_{vox,2}$ represent the range of its spatial expansion in the three-dimensional (3D) space, $\vec{r}' = \vec{r}_\rho - \vec{r}_T$, $\vec{r}'' = \vec{r}_\rho - \vec{r}_R$ and $\vec{r}_\rho$, $\vec{r}_T$, $\vec{r}_R$ denote the position vector of the voxel, and the position vector of the transmitter and receiver, respectively. Since $\rho(x,y,z)$ is zero in the rest of the space, (3) can be written as:

$$
\begin{aligned}
&E_{scatt}(x_R, y_R, x_T, y_T, f) \\
&= \int\int\int \rho(x,y,z) e^{-jk_{T,x}(x-x_T)-jk_{T,y}(y-y_T)-jk_{T,z}(z-z_T)} \\
&\quad \cdot e^{-jk_{R,x}(x-x_R)-jk_{R,y}(y-y_R)-jk_{R,z}(z-z_R)} dx dy dz \\
&= \alpha . \int\int\int \rho(x,y,z) e^{-jk_x x - jk_y y - jk_z z} dx dy dz \\
&= \alpha . P(k_x, k_y, k_z),
\end{aligned}
\tag{4}
$$

where $P(k_x, k_y, k_z)$ is the Fourier transform of the reflectivity function,

$$
\alpha = e^{jk_{T,x}x_T + jk_{T,y}y_T + jk_{T,z}z_T + jk_{R,x}x_R + jk_{R,y}y_R + jk_{R,z}z_R}, \tag{5}
$$

is a shifting factor and the rest of the parameters are defined as follows:

$$
\begin{aligned}
k_{T,y} &= k\sin(\theta_T)\cos(\varphi_T) \\
k_{R,y} &= k\sin(\theta_R)\cos(\varphi_R) \\
k_{T,z} &= k\sin(\theta_T)\sin(\varphi_T) \\
k_{R,z} &= k\sin(\theta_R)\sin(\varphi_R) \\
k_{T,x} &= k\cos(\theta_T) \\
k_{R,x} &= k\cos(\theta_R) \\
k_y &= k_{T,y} + k_{R,y} = k\sin(\theta_T)\cos(\varphi_T) + k\sin(\theta_R)\cos(\varphi_R) \\
k_z &= k_{T,z} + k_{R,z} = k\sin(\theta_T)\sin(\varphi_T) + k\sin(\theta_R)\sin(\varphi_R) \\
k_x &= k_{T,x} + k_{R,x} = k(\cos(\theta_T) + \cos(\theta_R)),
\end{aligned}
\tag{6}
$$

where $\theta_T, \varphi_T, \theta_R$ and φ_R are corresponding spherical coordinates of the transmitter and receiver, respectively. Hence, for a specific voxel of the object, each transmitter-receiver pair measures its Fourier transform at a specific frequency, i.e., (k_x, k_y, k_z) given by (6). This frequency varies from one voxel to another. Therefore, in a multi-static structure with one transmitter and an array of receivers, different frequency ranges would be detected for different voxels of the object.

As a simple clarification, the normal vector of surface variation (which denotes a k-space vector) at any voxel is measured by the TX/RX pair, whose location is such that, the bisector of the angle between that pair and the voxel lie along the aforementioned normal vector. However, if the bisector of multiple TX/RX pairs with reference to a specific voxel, lie along the same line, the measured back-scattered field includes redundant frequency information. As a consequence, there is no guarantee that the data measured by different TX/RX pairs, contain unique information [18].
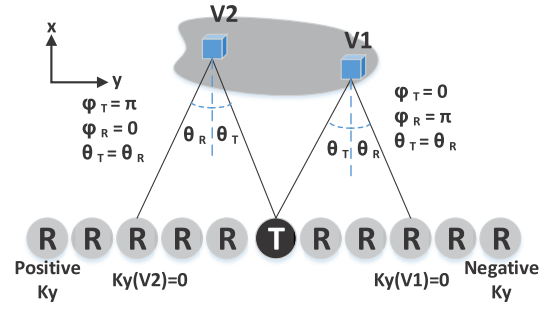

Fig. 3. *K*-space representation of multi-static arrays.

A. K-Space Representation of Multi-Static and Mono-Static Arrays

Herein after, for simplicity, we write our expressions in 2D space. Consider the multi-static array consisting of a central transmitter and multiple receivers, as shown in Fig. 3. For each specific object's voxel, according to (6), the receiver placed at position $\theta_R = \theta_T$ (also, $\cos(\varphi_T) = -\cos(\varphi_R)$ must hold), receives the zero frequency term of that voxel (note that, θ_T and θ_R are in spherical coordinates and thus are in the range of $[0, \pi]$. See Fig. 3 as an example). The receivers, placed before and after that receiver along the y axis, collect the Fourier transform of the voxel at positive and negative frequencies, respectively. Therefore, if we assume that the length of the aperture is limited, we will be measuring the Fourier transform of different voxels of the target at different frequency ranges. As can be seen in Fig. 3, for a voxel placed at furthest horizontal distance away from the transmitter, θ_T has the largest value in comparison to the respective angle of other voxels. In this case, the maximum frequency component is captured by the receiver located at furthest distance on the same side of the transmitter with respect to the voxel, i.e. the maximum θ_R. Since, $\sin(\theta_T)$ and $\sin(\theta_R)$ are maximum for that voxel and the aforementioned receiver, according to (6) the measured frequency sample is the maximum frequency-term of the system, which determines its bandwidth. The different frequency ranges measured from different voxels of the target indicates that sparse multi-static systems generally have distinct response to different shifted input impulses and thus are shift-varying.

In Mono-static arrays, the transceiver measures the zero-frequency term of the voxel that it directly points to. The transceiver also collects higher frequency-terms from the neighboring voxels in the range of $(-2k\sin(\theta_{obj,2}), 2k\sin(\theta_{obj,1}))$, where $\theta_{obj,1}$ and $\theta_{obj,2}$ are limited by the minimum of the beam-width of antenna and the viewing angle of the target [1]. If the aperture of the mono-static array is wide enough, the $(-2k\sin(\frac{\theta_{FBW}}{2}), 2k\sin(\frac{\theta_{FBW}}{2}))$ frequency range from all voxels of the target object will be collected, where θ_{FBW} is the full beam-width of antennas.

Sheen *et al.* did a study about the *k*-space model of multi-static arrays, but they mistook the *k*-space representation of mono-static arrays presented in [1], for that of a general imaging system. Similar to what is mentioned in this section about mono-static arrays (shown in Fig. 4), they considered the measured *k*-space span as $k_{incident} + (-k\sin(\theta_{obj,2}), k\sin(\theta_{obj,1}))$, but this is only the measured
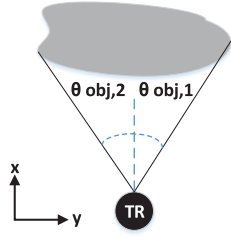
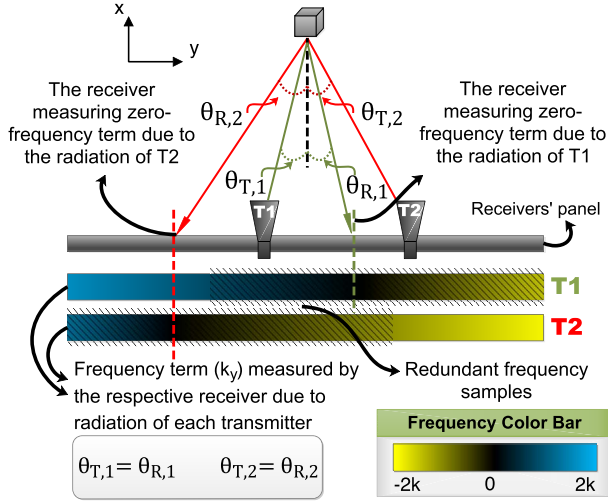Fig. 4. *K*-space representation of mono-static arrays.

Fig. 5. An example of redundancy in *k*-space domain.

data by the receiver placed at the transmitter's position, from different voxels of the object. In other words, they assumed that the range of the *k*-space is limited by the transmitter's viewing angle and neglected the role of the array size of receivers, in determining the measured *k*-space span of the target. Assuming the measured data is band-limited with the aforementioned bandwidth, they subsampled their receivers array, but in spite of their expectations, ended-up with an aliased image. They alleviated this problem by applying a bandpass filter, and justified it by explaining the role of bumps and holes, in expanding the measured spatial frequency span. Although, what they claimed is right, but it is justifiable only through the here-presented *k*-space analysis for multi-static structures. In other words, although such bumps and holes produce high frequency components, the bandwidth will be widened only if there are receivers in appropriate locations, to receive such high frequency terms.

III. K-SPACE AWARE SAR BACK-PROJECTION ALGORITHM

Consider a multi-static system with multiple transmitters and receivers (see Fig. 5 for an example in 1D space). Transmitters are activated one after another, and the back-scattered field of the active transmitter is measured by receivers. For any specific voxel, the measured data has redundancy in spectral domain, at a specific frequency range [18]. As shown in Fig. 5, according to (6), for a specific voxel in the space, the receiver located at the position where $\theta_{R,j} = \theta_{T,i}$ (also, $cos(\varphi_{T,i}) = -cos(\varphi_{R,j})$ must hold), measures the zero frequency-term of

that voxel, where i and j indicate the index number of the active transmitter and receiver, respectively. The measured spectrum of the voxel from the radiation of transmitters, T1 and T2, are depicted in the figure as a colorbar. It can be seen that, the frequency range indicated by hachure is in common among those spectrums. So, in this frequency span, the collected data of the voxel is redundant, while unique frequency samples are measured in the rest of the spectrum. Such redundancies, which depend on the position of transmitters, receivers and the voxel, are not distributed uniformly in the frequency domain and act as an undesirable filter, distorting the appearance of the imaging result [18]. In a given imaging system, regarding the number of times each frequency term is captured for a specific voxel, the measured frequency spectrum of that voxel is multiplied by a function, which depends on the voxel's position. We can predict this weighting function and modify the SAR-BP algorithm presented in (7), to compensate this filter for all voxels in the reconstruction aperture [18]. Considering the SAR-BP formula [24]:

$$\rho(x, y) = \sum_i \sum_j E_{scatt}(y_{T,i}, y_{R,j})$$
$$\cdot e^{jk\sqrt{(y-y_{T,i})^2+(x-x_{ant})^2}} \cdot e^{jk\sqrt{(y-y_{R,j})^2+(x-x_{ant})^2}}, \quad (7)$$

where x_{ant} is the position of the antenna array along x axis, (x, y) is the position of each voxel under the test and E_{scatt} is the measured scattered field by the corresponding receiver. We define $F(x, y, x_{ant}, y_T, y_R)$ as a function that determines the spatial Fourier frequency term of the voxel located at (x, y), measured by the receiver at (x_{ant}, y_R) due to the radiation of the transmitter at (x_{ant}, y_T). Assuming that $T(x, y, k)$ is the histogram function showing the number of times the spatial frequency-term, k, of the voxel located at (x, y) is measured, the weighting function can be applied as follows [18]:

$$\rho(x, y) = \sum_i \sum_j E_{scatt}(y_{T,i}, y_{R,j})$$
$$\cdot T(x, y, F(x, y, x_{ant}, y_{T,i}, y_{R,j}))^{-1}$$
$$\cdot e^{jk\sqrt{(y-y_{T,i})^2+(x-x_{ant})^2}} \cdot e^{jk\sqrt{(y-y_{R,j})^2+(x-x_{ant})^2}}. \quad (8)$$

Applying and generating these functions are computationally expensive due to floating point error and non-uniform sampling in *k*-space domain, as described in [18]. In [18] applying (8) in multi-static imaging is studied, which is called precise k-space SAR back-projection algorithm (P-KA-SAR-BP) hereafter. In this paper we introduce an approximation of (8) to alleviate its high computational cost. Assuming that the object is far enough, a small angle approximation can be considered for function F, by substituting $sin(\theta)$ by $tan(\theta)$ in (6) as follows:

$$F(x, y, x_{ant}, y_T, y_R) = k_y(\theta_T, \varphi_T, \theta_R, \varphi_R)$$
$$= ksin(\theta_T)cos(\varphi_T) + ksin(\theta_R)cos(\varphi_R)$$
$$\approx ktan(\theta_T)cos(\varphi_T) + ktan(\theta_R)cos(\varphi_R)$$

$$= k\frac{|y - y_T|}{x - x_{ant}} \times \frac{y - y_T}{|y - y_T|}$$
$$+ k\frac{|y - y_R|}{x - x_{ant}} \times \frac{y - y_R}{|y - y_R|}$$
$$= \beta((y - y_T) + (y - y_R)), \quad (9)$$

where $\beta = k/(x - x_{ant})$ for any given voxel at (x, y), and $\theta_T, \varphi_T, \theta_R, \varphi_R$ are corresponding spherical coordinates of the transmitter and receiver, as shown in Figs. 1 and 3.

Given that y_R is uniformly sampled, the approximation used in (9) helps to consider uniform sampling intervals in k-space domain. Moreover, in spite of (6), which is used to find $F(x, y, x_{ant}, y_{T,i}, y_{R,j})$ in (8), (9) is free of trigonometric functions, that alleviates the floating point error problem of computing $F(x, y, x_{ant}, y_T, y_R)$. Specially, if y, y_T and y_R are multiples of a step like δ_y, (9) can be written as:

$$F(x, y, x_{ant}, y_T, y_R) = \beta((y - y_T) + (y - y_R))$$
$$= \beta\delta_y((\frac{y}{\delta_y} - \frac{y_T}{\delta_y}) + (\frac{y}{\delta_y} - \frac{y_R}{\delta_y}))$$
$$= \beta\delta_y((Y - Y_T) + (Y - Y_R)) \quad (10)$$

where $Y = y/\delta_y$, $Y_T = y_T/\delta_y$, $Y_R = y_R/\delta_y$ and $\beta\delta_y$ is constant. If $\beta\delta_y$ is omitted from (10), the rest of the equation only consists of integer numbers, that absolutely solves the floating point error problem of finding (9). As a result, the complexity of finding redundant frequency samples and thus generating function $T(x, y, k)$ can be simplified.

In the rest of the paper we use this approximated algorithm, whose efficiency is also reported in Section VI.

IV. THE EFFECTIVE APERTURE CONCEPT

The effective aperture concept approximates the behavior of multi-static arrays by its far-field characteristics [15]. This approach that was first introduced in ultrasonic imaging [17], considers the convolution of the transmitter and receiver arrays as the effective aperture of the imaging system [17]. This effective aperture can be regarded as the equivalent mono-static imaging array that generates the identical radiation pattern [17]. The array factors of the receiver ($P_R(f)$) and transmitter ($P_T(f)$) arrays, which is given by the Fourier transform of each array's aperture function [17], can be defined as:

$$P_R(f) = \int_{-\infty}^{\infty} a_R(y)e^{i2\pi fy}dy$$
$$P_T(f) = \int_{-\infty}^{\infty} a_T(y)e^{i2\pi fy}dy \quad (11)$$

where, y represents the antennas' location divided by the wavelength and $a_R(y)$ and $a_T(y)$ are the aperture functions of the receiver and transmitter arrays, respectively. The two-way radiation pattern [17] in the far-field can be defined as:

$$P_{TR}(f) = P_T(f)P_R(f). \quad (12)$$

The inverse Fourier transform of (12) is called the effective aperture ($E(y)$) [17], that can be calculated by convolving the aperture function of transmitter and receiver arrays as follows:
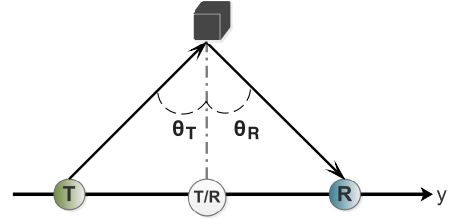
$$E(y) = a_T(y) \circledast a_R(y). \quad (13)$$

Fig. 6. The relationship between the k-space analysis and the effective aperture concept.

Since, convolution is a linear operator, we can study each antenna element in the array independently. Consider a transmitter positioned at y_T and a receiver positioned at y_R. The aperture functions and the two-way radiation pattern can be found as:

$$P_R(f) = \int_{-\infty}^{\infty} \delta(y - y_R)e^{i2\pi fy}dy = e^{i2\pi fy_R}$$
$$P_T(f) = \int_{-\infty}^{\infty} \delta(y - y_T)e^{i2\pi fy}dy = e^{i2\pi fy_T}$$
$$P_{TR}(f) = P_T(f)P_R(f) = e^{i2\pi fy_T}e^{i2\pi fy_R} = e^{i2\pi f(y_T+y_R)}. \quad (14)$$

Assume that, the equivalent mono-static Tx/Rx pair in the corresponding effective aperture, is positioned at y_e. So, its aperture function ($P_E(f)$) and the two-way radiation pattern ($P_{E,TR}(f)$) can be found as:

$$P_E(f) = \int_{-\infty}^{\infty} \delta(y - y_e)e^{i2\pi fy}dy = e^{i2\pi fy_e}$$
$$P_{E,TR}(f) = P_E(f)P_E(f) = e^{i2\pi fy_e}e^{i2\pi fy_e} = e^{i2\pi f(2y_e)}. \quad (15)$$

The effective aperture yields the identical radiation pattern in the far-field. So, from (14) and (15) we obtain:

$$P_{TR}(f) = P_{E,TR}(f)$$
$$e^{i2\pi f(y_T+y_R)} = e^{i2\pi f(2y_e)}, \quad (16)$$
$$\delta(y - y_T) \circledast \delta(y - y_R) = \delta(y - 2y_e), \quad (17)$$

from (16) it can be seen that, $y_e = \frac{(y_T+y_R)}{2}$. It means that, the effective aperture concept considers an equivalent Tx/Rx element at the middle of any Tx/Rx pairs. Also, (17) shows that the position of elements in the effective aperture expression shown in (13) should be divided by two to represent the equivalent mono-static aperture. The reason behind this is that as opposed to (11) (which represents one-way aperture functions), (12) is a two-way aperture function that requires the effective aperture shown in (13) be squeezed by a factor of 2 to represent the equivalent mono-static array. Consider the two transmitter and receiver antennas in Fig. 6, showing a voxel placed at their perpendicular bisector. Also, the equivalent Tx/Rx antenna is shown as T/R in the figure. As shown in Section III, the mirror-like reflection where $\theta_T = \theta_R$, results in zero frequency term in the k-space domain. Because θ_T and θ_R are zero for the equivalent Tx/Rx antenna, it also collects the zero frequency term from the voxel. Since, this holds for any transmitter-receiver pair, it can be concluded that the effective aperture concept is just a guarantee of capturing

the zero frequency component from all voxels. Still, frequency components are captured non-uniformly from different voxels. The new approach proposed in this paper, is therefore, a generalized effective aperture, where the placement and rotation of antennas in the sparse array is determined in a way to widen the measured frequency span from different voxels that also, results in a more uniform acquisition of frequency components from imaging voxels.

V. THE PROPOSED SUPER-RESOLUTION METHOD

In the proposed method, we aim to expand the measured k-space range associated with each voxel and reduce the redundancy in the collected frequency components, to more uniformly capture the spatial frequency band. Here, the frequency means the rate of changes and thus, higher frequency terms are associated with abrupt changes in intensity such as what happens in edges. As a result, collecting higher frequency terms leads to sharper edges in the recovered image. The relation between the k-space measured frequency span and the resolution for any voxel in the imaging aperture is approximately as follows [9]:

$$\delta_x = \frac{2\pi}{\Delta k_x}$$
$$\delta_y = \frac{2\pi}{\Delta k_y}$$
$$\delta_z = \frac{2\pi}{\Delta k_z}. \tag{18}$$

In practical imaging systems, the beam-width of antennas is limited. Using wide beam antennas, leads to a poor imaging quality due to low antennas' gain, fluctuations in antennas' gain and the coupling effect of antennas [25]. So, we should find a way to design efficient arrays based on this limitation. Assume that, there are an array of receivers along with three transmitters. We are going to measure the widest spectral bandwidth from the target using this antenna array. Let us also consider a specific region where the target of interest (TOI) may exist, named as the region of interest (ROI). The conventional structure with a specific ROI is shown in Fig. 7(a). In this structure, receivers are placed every $\frac{\lambda}{2}$ and three transmitters are placed at the center of the receivers' array and its two ends. The transmitter antennas' pattern indicating their beam-width is shown in the figure. Based on (6), in order to measure the maximum frequency term (k_y) from the TOI, both θ_T and θ_R should be maximized (figures 3 and 1 include a hint on the value of φ_T and φ_R in (6)). In this structure the maximum frequency term is either measured from the voxel entitled $V1$ by the left side receiver and the central transmitter:

$$k_{y,max}(V1) = ksin(\theta_{1T}) + ksin(\theta_{1R}), \tag{19}$$

or from peripheral voxels, e.g. $V2$, by the right transmitter and left receiver:

$$k_{y,max}(V2) = ksin(\theta_{2R}) - ksin(\theta_{2T}). \tag{20}$$

Depending on the beam-width of transmitters, $k_{y,max}(V2)$ can be smaller than $k_{y,max}(V1)$. Therefore, in such a multi-static system the side transmitters may only help to
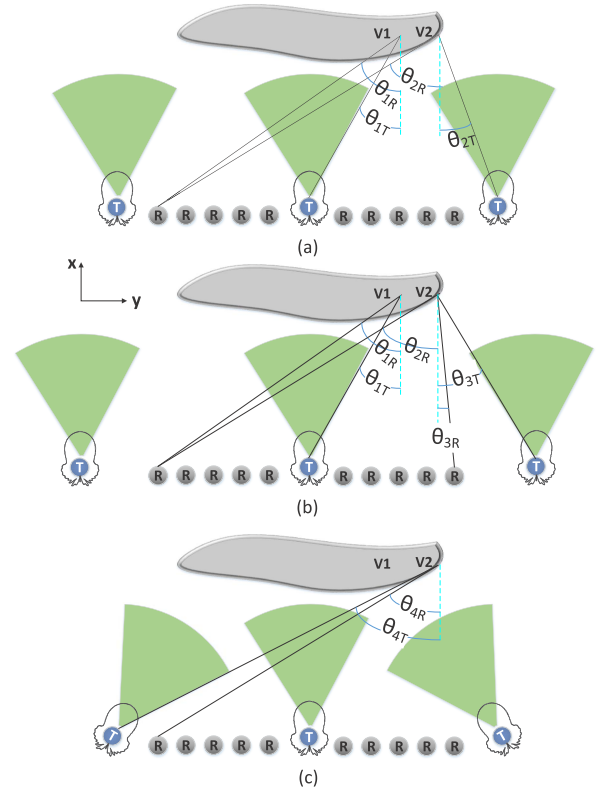

Fig. 7. Comparing a conventional multi-static array and an array based on the proposed design. Central transmitter illuminates V1 in (a)–(c). Left transmitter illuminates V1 and V2 only in (c). Right transmitter illuminates V1 in (a) and (c) and V2 in (a)–(c). (a) A conventional Multi-static structure. (b) Enlarging transmitter's array. (c) Rotating transmitters.

extend the effective aperture of imaging and don't help much in improving the overall measured spectral span of the TOI. One solution can be to enlarge the transmitter's array as shown in Fig. 7(b). The maximum frequency term captured from $V2$ in this case is:

$$k_{y,max}(V2) = ksin(\theta_{2R}) - ksin(\theta_{3T}). \tag{21}$$

This solution actually degrades the maximum frequency term of $V2$ because comparing (21) and (20), θ_{3T} is greater than θ_{2T} while θ_{2R} remains constant. Although, the maximum negative frequency captured from $V2$ will be improved, which can be obtained as:

$$k_{y,max,negative}(V2) = -ksin(\theta_{3R}) - ksin(\theta_{3T}), \tag{22}$$

the absolute value of this frequency term is still much lower than the $k_{y,max}(V1)$ and $k_{y,max}(V2)$ shown in (19) and (20), respectively and can't become higher than that. In other words moving the side transmitters away only shifts the measured spectral spectrum of the voxels placed in their field of view. This shift is not much useful because this movement, also moves the radiation beam of side transmitters away from the ROI.

To alleviate this problem, in this paper, we propose to rotate the side transmitters such that their beam can reach the voxel on the farthest side in the ROI as shown in Fig. 7(c). Employing this technique, the high inclined angle of transmitter's beam results in large value of θ_T in (6) and consequently
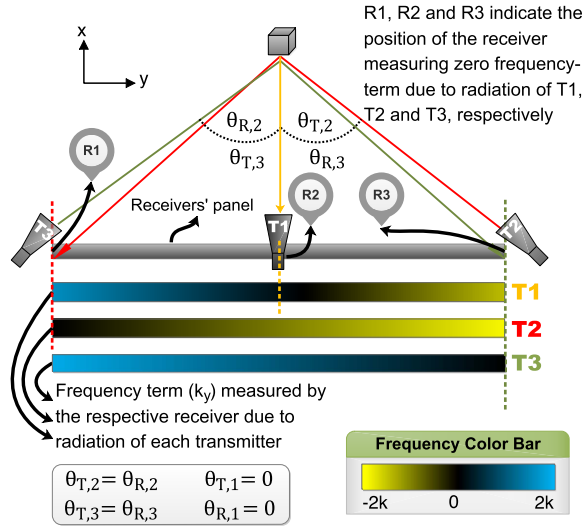
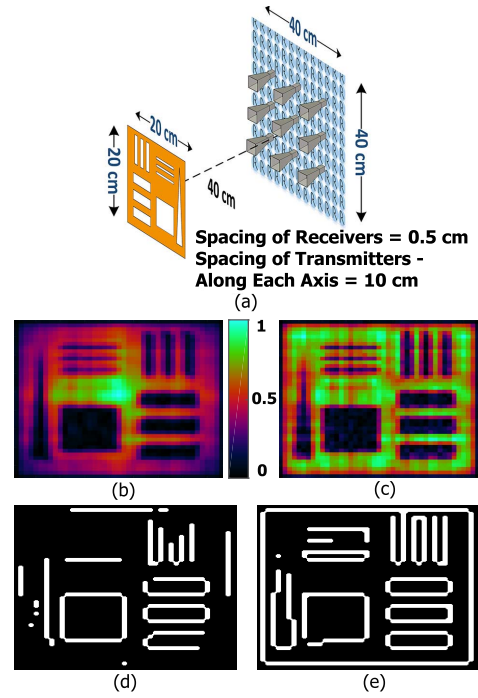Fig. 8. The proposed structure: rotating antennas' beam.

Fig. 9. Simulation of a multi-static setup with direct beam transmitters. (a) Imaging setup. (b) The result using the SAR-BP. (c) The result using the KA-SAR-BP. (d) Edge of Fig. 9(b). (e) Edge of Fig. 9(c).

improves the maximum captured frequency term from all voxels of the target placed at transmitters' new field of view. Also, the rotation and enlargement of the transmitters' array together, can even more increase θ_T in (6) and considerably improve the captured spectral bandwidth and thus the resolution of imaging. The maximum measured frequency in Fig. 7(c) can be obtained as:

$$k_{y,max,Rotated} = k sin(\theta_{4R}) + k sin(\theta_{4T}), \qquad (23)$$

which is much higher than that of conventional array shown in (19).

The modified configuration of multi-static arrays is also studied for a single voxel as shown in Fig. 8. It can be noticed that, if we move the transmitter T2 of Fig. 5 further away from the center, and rotate it such that the main lobe of its beam can cover the intended voxels in the imaging aperture, higher frequency terms of these voxels can be obtained in comparison to Fig. 5, which is depicted in the respective colorbars. Given that the collected spectral data measured by the receivers due to radiation of T2 mostly covers one side of the spectrum of the image voxels, another transmitter, T3, is placed at the other side to measure frequency terms at the other side of the spectrum. Moreover, a central transmitter is placed to ensure that enough low frequency samples are measured from all voxels in the imaging aperture.

Therefore, in a practical imaging system consisting of three transmitters, if a couple of transmitters, placed at the sides, are rotated in a way that their beam can cover most voxels of the aperture in inclined incident angles and a central transmitter is considered to measure low frequency samples from all voxels, then not only less redundant data is collected but also higher frequency terms that contain edge information will be measured.

Having said that, rotating the transmitters at the sides, prevents collecting low-frequency terms from voxels at the aperture sides. Still, low-frequency terms contain the overall structure of the reconstructed image, and this leads to a poor quality of the image in such regions. Thus, the effective aperture of the system would be decreased. To alleviate this problem, some transmitters that are not rotated, can be placed at the sides, to help collecting low frequency samples. So, based on these considerations, more complex multi-static arrays can be designed to fulfill the requirements of any multi-static imaging systems.

In the rest of the paper, for simplicity, it is assumed that receivers have wide enough beam pattern, that they can measure all necessary information. Considering the receivers to have real beam-width, imposes a limitation on the enhancement we expect from systems. Nevertheless, the system with rotated transmitters, still performs better than the one with direct transmitters, as will be shown in the experimental measurement in the following section.

VI. EXPERIMENTS AND SIMULATIONS

Simulations and a couple of experimental measurements are performed to verify the effectiveness of the proposed method. In all three simulations, the frequency is set at 30 GHz. Horn antennas with 60 degree beam-width and point-source antennas are used as transmitters and receivers, respectively. The receivers' panel size is 40×40 cm^2. The spacing between receivers is 5 mm, so the panel consists of 81×81 receivers. Also, the simulation setup for different simulations are shown in Figs. 9(a), 10(a) and 11(a).

In all considered simulations, a resolution chart is chosen as the input target due to its variable spatial frequency contents. Furthermore, the transmitters are placed in a 2D style. To ensure that transmitters' beam can cover the object, in the first simulation structure, i.e. Fig. 9(a), transmitters are placed in front of the corners and the center of the object. Similarly, in
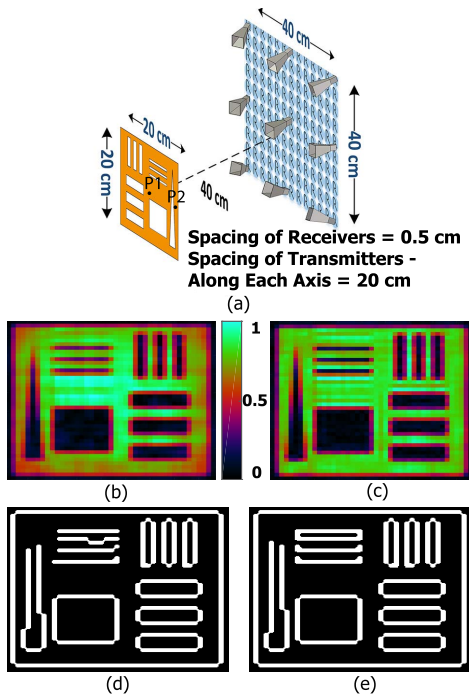
Fig. 10. Simulation of a multi-static setup with rotated beam transmitters. (a) Imaging setup. (b) The result using the SAR-BP. (c) The result using the KA-SAR-BP. (d) Edge of Fig. 10(b). (e) Edge of Fig. 10(c).
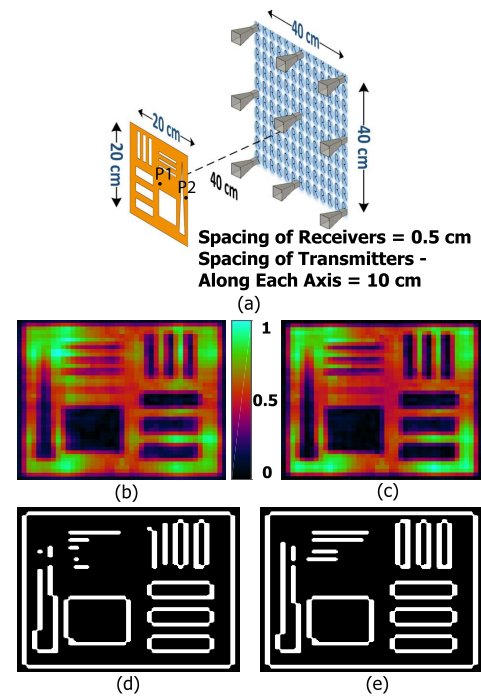

Fig. 11. Simulation of a multi-static setup with large array of transmitters. (a) Imaging setup. (b) The result using the SAR-BP. (c) The result using the KA-SAR-BP. (d) Edge of Fig. 11(b). (e) Edge of Fig. 11(c).

the second simulation shown in Fig. 10(a), transmitters are rotated such that their beam can cover the most distant voxels of the object in an inclined incident angle, in order to capture high frequency components. In this simulation, all transmitters are pointing to the center of the object. The third simulation is done to show the ineffectiveness of the aperture size (like the case analyzed in Fig. 7(b)) in comparison of conventional arrays and the proposed one. The simulation setup is shown in Fig. 11(a). In this simulation, transmitters are placed at the sides of receivers' array but with no rotation. The imaging results for three structures using the SAR-BP, are shown in Figs. 9(b), 10(b) and 11(b), also their respective edges are shown in Figs. 9(d), 10(d) and 11(d), respectively. Moreover, the results using the KA-SAR-BP are shown in Figs. 9(c), 10(c) and 11(c) for three imaging structures, and their edges are shown in Figs. 9(e), 10(e) and 11(e), respectively. From these results it can be seen that the quality of images in the proposed structure is superior to conventional multi-static arrays, and the edges of narrower strips are better preserved. Also, the KA-SAR-BP algorithm has considerably enhanced the imaging quality, leading to sharper edges, in comparison to the conventional SAR-BP algorithm. But comparing Figs. 11(b) and 11(c), it can be seen that in spite of our expectations, uniform regions are slightly better preserved using SAR-BP than KA-SAR-BP. The reason is that the transmitters are placed such away from the object that, the fluctuation in antennas' beam has prevented KA-SAR-BP to improve uniform regions.

Experimental measurements are also performed to validate the effectiveness of the proposed method in practical structures. Similar to the simulations, a set of two measurements

are done. In the first measurement, shown in Fig. 12(a), three transmitters are placed horizontally in front of the center and edges of the object. Due to practical limitations, transmitters are placed under the aperture of receivers and their beam are rotated vertically to cover the object [18]. In the second scenario shown in Fig. 13(a), three transmitters are placed horizontally in the center and corners of the receivers' aperture, and rotated toward the center of the object. A Vector network analyzer (VNA) is used for measurements that has maximum working frequency of 40 GHz. In both measurements, the imaging setup operates in frequency band of 27-31 GHz with 51 equally-spaced frequency steps. In order to achieve enough beam-width and gain, a Vivaldi antenna with 11 dB gain is used as the receiver. The aperture size is 40×35 cm^2, and the receiver sweeps the aperture mechanically, sampling every 0.5 cm. Also, a Horn antenna with 20 dB gain is chosen as the transmitter to generate enough power, which is manually placed at the aforementioned positions. The recovered images using the SAR-BP and KA-SAR-BP algorithms of the first measurement, are shown in Figs. 12(b) and 12(c), respectively. Moreover, the respective edges are shown in Figs. 12(d) and 12(e). Also, Figs. 13(b) and 13(c) represent the reconstructed images of the second measurement using the SAR-BP and the KA-SAR-BP algorithms, respectively and again, the respective edges are shown in Figs. 13(d) and 13(e). As already mentioned, the edges are extracted by using a Sobel mask filter, and the same threshold is applied on all images.

From these results it can be seen that, in the first measurement (see Fig. 12), although a shadow of two narrower strips at the right side of the object, can be seen in Figs. 12(b) and 12(c), both algorithms failed in efficiently
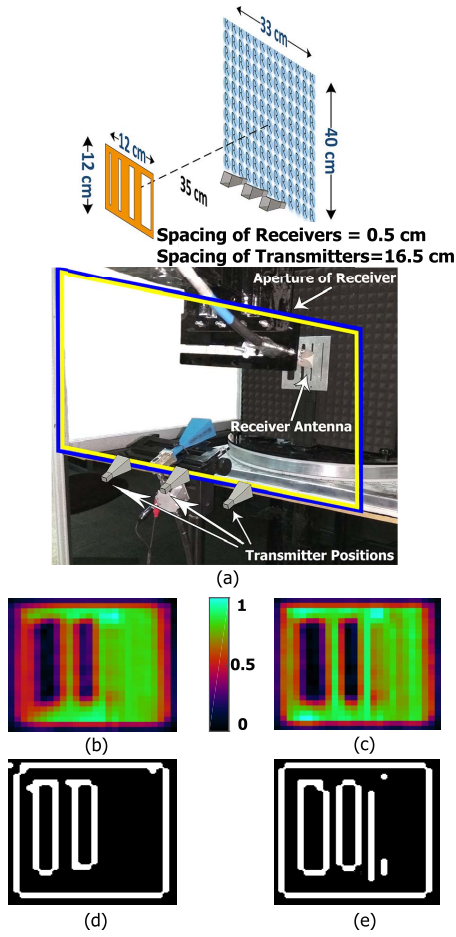
Fig. 12. Multi-static experimental setup with direct beam transmitters. (a) Imaging setup. (b) The result using the SAR-BP [18]. (c) The result using the KA-SAR-BP. (d) Edge of Fig. 12(b). (e) Edge of Fig. 12(c).
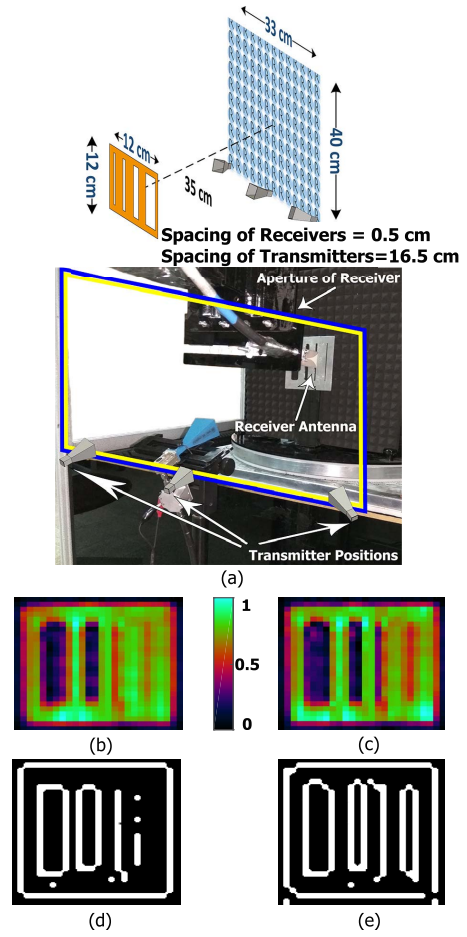

Fig. 13. Multi-static experimental setup with rotated beam transmitters. (a) Imaging setup. (b) The result using the SAR-BP. (c) The result using the KA-SAR-BP. (d) Edge of Fig. 13(b). (e) Edge of Fig. 13(c).

recovering these strips. On the other hand, the second measurement validates the performance of the proposed structure in preserving narrower strips and thus higher frequency components, as shown in Fig. 13. All edges are recovered in the result of the SAR-BP algorithm as seen in Figs. 13(b) and 13(d), but the narrowest strip at the right side of the object, is not sharp enough to be extracted completely by the Sobel mask. Moreover, Figs. 13(c) and 13(e) validate the effectiveness of the KA-SAR-BP algorithm, in which, the narrowest strip is recovered sharp enough to be detected by the Sobel mask.

Comparing Figs. 12(b) by 12(c) and 13(b) by 13(c), it can be seen that uniform regions are improved in the images recovered by the KA-SAR-BP algorithm in comparison to those recovered by the SAR-BP. This uniformity is not as clear as some simulation results, such as Fig. 9(b) compared to Fig. 9(c). The reason is that as can be seen in [18, Fig. 5] in a setup with three transmitters, the distortion effect of redundant spectral data in uniform regions, is not considerable. Also, the reason can be the narrow beam-width and the amplitude variation of the real transmitter and receiver antennas' beam that made this uniformity less clear.

As discussed in Section II, the sparse multi-static systems are shift-varying. So the PSF of systems varies from one point

to another point. So, we study the PSF of the system at two different points, i.e. the center and the corner of the object in the simulations shown in Figs. 10 and 11 labeled as P1 and P2, respectively. The results are shown in Fig. 14. The frequency is set at 28-32 GHz with 21 equally spaced samples. The lateral and depth cut of the impulse located at P1 are shown in Figs. 14(a) and 14(b) and the lateral and depth cut of the impulse located at P2 are shown in Figs. 14(c) and 14(d), respectively. From these results it can be seen that the results of the proposed array with the SAR-BP algorithm is superior than that of the conventional array with SAR-BP algorithm in terms of resolution and side lobe level. Moreover, comparing the results of the proposed array using SAR-BP and KA-SAR-BP, it can be seen that, although the redundancy compensation improves the quality and resolution of images, it degrades the side lobe level of the PSF.

In this paper we proposed the KA-SAR-BP algorithm to alleviate the computational complexity of P-KA-SAR-BP presented in [18], and presented all our results based on KA-SAR-BP. Also, we have reconstructed all measurements and simulations using the P-KA-SAR-BP algorithm as well, as shown in Fig. 15. The reconstructed images using P-KA-SAR-BP of simulations and measurements displayed

Conventional Array reconstructed using SAR-BP
The proposed array reconstructed using SAR-BP
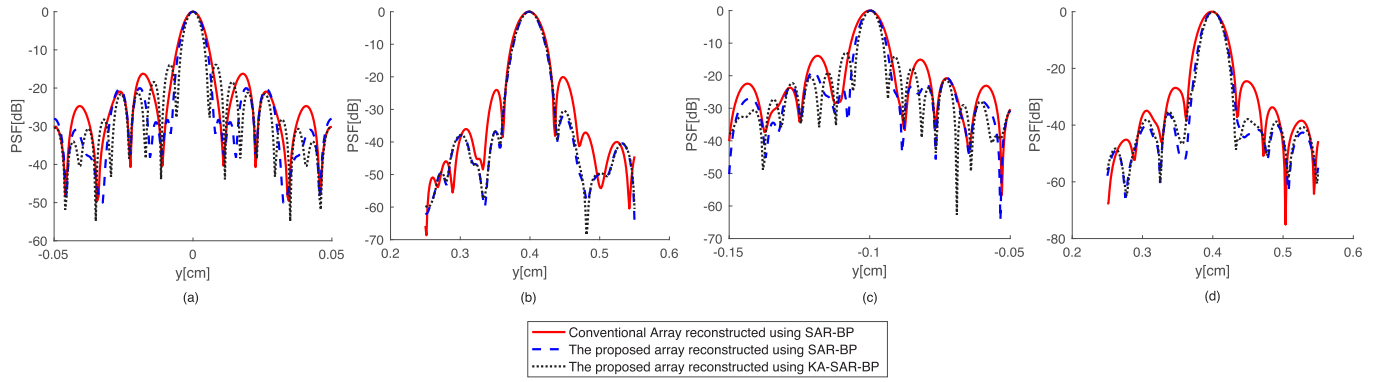The proposed array reconstructed using KA-SAR-BP

Fig. 14. PSF of the systems shown in Figs. 10 and 11 at points labeled P1 and P2. (a) Lateral cut at P1. (b) Depth cut at P1. (c) Lateral cut at P2. (d) Depth cut at P2.
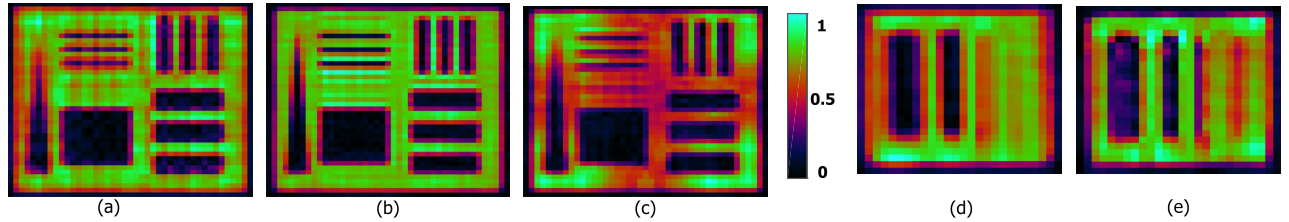

Fig. 15. Reconstruction using P-KA-SAR-BP of the simulations and measurement shown in: (a) Fig. 9; (b) Fig. 10; (c) Fig. 11; (d) Fig. 12 [18]; (e) Fig. 13.

TABLE I

QUANTITATIVE RESULTS

Type	Figure Number	Reconstruction Algorithm	PSNR	SSIM	DIC
Simulation	Fig. 9	SAR-BP	7.1767	0.4588	0.6865
		P-KA-SAR-BP	11.3988	0.6271	0.8677
		KA-SAR-BP	11.2031	0.5874	0.8642
	Fig. 10*	SAR-BP	11.1983	0.6422	0.8450
		P-KA-SAR-BP	11.4876	0.6694	0.8842
		KA-SAR-BP	11.8694	0.6804	0.8822
	Fig. 11	SAR-BP	9.1524	0.4854	0.7794
		P-KA-SAR-BP	8.6368	0.5075	0.7910
		KA-SAR-BP	8.7575	0.5088	0.7873
Measurement	Fig. 12	SAR-BP	8.1160	0.2791	0.5604
		P-KA-SAR-BP	8.8336	0.3745	0.7015
		KA-SAR-BP	9.3052	0.3868	0.6959
	Fig. 13*	SAR-BP	9.4682	0.4572	0.7361
		P-KA-SAR-BP	9.5466	0.5159	0.7736
		KA-SAR-BP	9.7878	0.5240	0.7798

* The proposed structure.

in Figs. 9(a), 10(a), 11(a), 12(a) and 13(a) are shown in Figs. 15(a), 15(b), 15(c), 15(d) and 15(e). The images are similar, so quantitative metrics should be exploited for comparison.

Quantitative metrics are also used to verify the proposed structure and algorithm. Three quality metrics, i.e., PSNR [26], SSIM [27] and DIC [26] are used to compare the obtained results of simulations and measurements, as shown in Table I. The quality metrics presented in Table I,

are measured based on the comparison of the obtained results over manually generated ideal reference images. The PSNR metric is based on pixel differences. It measures the ratio of the peak power of the signal to the mean square error of the image and the reference, which is equivalent to the power of the noise. The DIC is a correlation based metric and determines the similarity between two images. Thus, such kind of measures are complementary to pixel-difference based type of measures [26]. The SSIM is a perception based model that is proposed to improve traditional measures that are based on the comparison of images pixel by pixel, e.g., PSNR and DIC. In addition to pixel-wise comparison, SSIM also, includes the inter dependencies among pixels [27]. The use of KA-SAR-BP and P-KA-SAR-BP algorithm has improved all quality metrics. There is only one exception that SAR-BP has led to a better PSNR in simulations, pertaining to Fig. 11. As already discussed in Section V, the reason being that, in that simulation the large array of the transmitters and consequently the beam amplitude variation of transmitters has prevented KA-SAR-BP and P-KA-SAR-BP to improve uniform regions. But, the superiority of SSIM and DIC metrics for KA-SAR-BP and P-KA-SAR-BP algorithms in results of Fig. 11, prove their effectiveness. It should be here mentioned that, in some set of simulations the metrics for the proposed array reconstructed by the SAR-BP is not better than those of the conventional array using the KA-SAR-BP (see PSNR and DIC metrics in the results of simulations of Table I). Still, the proposed structure is superior to simple arrays in terms of all the aforementioned metrics, if the same reconstruction algorithm is used. The KA-SAR-BP algorithm improves PSNR, SSIM and DIC metrics, with an average value of 1.16 dB, 0.073 and 0.081, respectively. The improvement of P-KA-SAR-BP algorithm is 0.96 dB, 0.074 and 0.082, for PSNR, SSIM and

DIC metrics, respectively. This shows that the efficiency of both algorithms is similar and even the proposed KA-SAR-BP in this paper, even though simpler in implementation, shows better results in many cases than P-KA-SAR-BP. Also, using the same reconstruction algorithm, the proposed structure leads to 1.22 dB, 0.13 and 0.087 improvement in PSNR, SSIM and DIC, respectively. All in all, the proposed method improves PSNR, SSIM and DIC metrics an average value of 3.03 dB, 0.22 and 0.173, respectively.

VII. Conclusion

A novel multi-static millimeter-wave imaging structure and reconstruction algorithm were proposed in order to improve the resolution and the overall spectral bandwidth of the reconstructed images. The measured frequency components for each voxel of the target was determined via the system's k-space representation. This information was then utilized to improve the multi-static imaging result through the KA-SAR-BP algorithm. The structure was also modified by rotating the transmitters, in order to measure higher spatial frequency terms over the voxels of the target. The resultant improvement in the image's resolution and spectral bandwidth, were validated through a number of simulations and experiments. The improved multi-static structure were simulated for a resolution chart target, demonstrating significant quality and high frequency features enhancement. The improvement in image resolution were demonstrated more specifically via imaging two object points. The resultant improved resolution and the lower side lobe levels confirmed the efficiency of the proposed structure. Finally, experimental measurements performed with the proposed and conventional multi-static structures, confirmed the effectiveness of the proposed structure and algorithm in practical experiments.

References

[1] D. M. Sheen, D. L. McMakin, and T. E. Hall, "Three-dimensional millimeter-wave imaging for concealed weapon detection," *IEEE Trans. Microw. Theory Techn.*, vol. 49, no. 9, pp. 1581–1592, Sep. 2001.

[2] V. M. Patel, J. N. Mait, D. W. Prather, and A. S. Hedden, "Computational millimeter wave imaging: Problems, progress, and prospects," *IEEE Signal Process. Mag.*, vol. 33, no. 5, pp. 109–118, Sep. 2016.

[3] J. C. Weatherall, J. Barber, and B. T. Smith, "Spectral signatures for identifying explosives with wideband millimeter-wave illumination," *IEEE Trans. Microw. Theory Techn.*, vol. 64, no. 3, pp. 999–1005, Mar. 2016.

[4] S. Kwon and S. Lee, "Recent advances in microwave imaging for breast cancer detection," *Int. J. Biomed. Imag.*, vol. 2016, Oct. 2016, Art. no. 5054912.

[5] P. Mehta, K. Chand, D. Narayanswamy, D. G. Beetner, R. Zoughi, and W. V. Stoecker, "Microwave reflectometry as a novel diagnostic tool for detection of skin cancers," *IEEE Trans. Instrum. Meas.*, vol. 55, no. 4, pp. 1309–1316, Aug. 2006.

[6] S. Oka, S. Mochizuki, H. Togo, and N. Kukutsu, "Inspection of concrete structures using millimeter-wave imaging technology," NTT, Tokyo, Japan, Tech. Rev. 7, 2009.

[7] D. M. Sheen, D. L. McMakin, and T. E. Hall, "Combined illumination cylindrical millimeter-wave imaging technique for concealed weapon detection," *AeroSense, Int. Soc. Opt. Photon.*, pp. 52–60, Jul. 2000.

[8] Y. Alvarez *et al.*, "Fourier-based imaging for multistatic radar systems," *IEEE Trans. Microw. Theory Techn.*, vol. 62, no. 8, pp. 1798–1810, Aug. 2014.

[9] S. S. Ahmed, A. Schiessl, F. Gumbmann, M. Tiebout, S. Methfessel, and L. Schmidt, "Advanced microwave imaging," *IEEE Microw. Mag.*, vol. 13, no. 6, pp. 26–43, Sep. 2012.

[10] J. Gao, Y. Qin, B. Deng, H. Wang, and X. Li, "Novel efficient 3D short-range imaging algorithms for a scanning 1D-MIMO array," *IEEE Trans. Image Process.*, vol. 27, no. 7, pp. 3631–3643, Jul. 2018.

[11] X. Zhuge and A. G. Yarovoy, "Three-dimensional near-field MIMO array imaging using range migration techniques," *IEEE Trans. Image Process.*, vol. 21, no. 6, pp. 3026–3033, Jun. 2012.

[12] R. Zhu, J. Zhou, L. Tang, Y. Kan, and Q. Fu, "Frequency-domain imaging algorithm for single-input–multiple-output array," *IEEE Geosci. Remote Sens. Lett.*, vol. 13, no. 12, pp. 1747–1751, Dec. 2016. doi: 10.1109/LGRS.2016.2602442.

[13] R. Zhu, J. Zhou, G. Jiang, and Q. Fu, "Range migration algorithm for near-field MIMO-SAR imaging," *IEEE Geosci. Remote Sens. Lett.*, vol. 14, no. 12, pp. 2280–2284, Dec. 2017.

[14] Y. Álvarez, Y. Rodriguez-Vaqueiro, B. Gonzalez-Valdes, F. Las-Heras, and A. García-Pino, "Fourier-based imaging for subsampled multistatic arrays," *IEEE Trans. Antennas Propag.*, vol. 64, no. 6, pp. 2557–2562, Jun. 2016.

[15] S. S. Ahmed, *Electronic Microwave Imaging With Planar Multistatic Arrays*. Berlin, Germany: Logos Verlag, 2014.

[16] P. M. Sanam, M. J. S. Talebi, M. Kazemi, Z. Kavehvash, and M. Shabany, "Thorough approach toward cylindrical MMW image reconstruction using sparse antenna array," *IET Image Process.*, vol. 12, no. 8, pp. 1458–1466, Aug. 2018.

[17] G. R. Lockwood and F. S. Foster, "Optimizing sparse two-dimensional transducer arrays using an effective aperture approach," in *Proc. IEEE Ultrason. Symp. (ULTSYM)*, Oct./Nov. 1994, pp. 1497–1501.

[18] M. Kazemi, M. Shabany, and Z. Kavehvash, "Spectral redundancy compensation in multi-static millimeter-wave imaging," *IEEE Trans. Circuits Syst. II, Exp. Briefs*, vol. 65, no. 5, pp. 687–691, May 2018.

[19] B. Gonzalez-Valdes, Y. Alvarez, S. Mantzavinos, C. M. Rappaport, F. Las-Heras, and J. Á. Martínez-Lorenzo, "Improving security screening: A comparison of multistatic radar configurations for human body imaging," *IEEE Antennas Propag. Mag.*, vol. 58, no. 4, pp. 35–47, Aug. 2016.

[20] C. V. J. Jakowatz, D. E. Wahl, P. H. Eichel, D. C. Ghiglia, and P. A. Thompson, *Spotlight-Mode Synthetic Aperture Radar: A Signal Processing Approach*. New York, NY, USA: Springer, 1996.

[21] C.-H. Tseng and T.-H. Chu, "Improvement of quasi-monostatic frequency-swept microwave imaging of conducting objects using illumination diversity technique," *IEEE Trans. Antennas Propag.*, vol. 53, no. 1, pp. 305–312, Jan. 2005.

[22] M. Soumekh, *Fourier Array Imaging*. Upper Saddle River, NJ, USA: Prentice-Hall, 1994.

[23] P. Morse and H. Feshbach, *Methods of Theoretical Physics*. New York, NY, USA: McGraw-Hill, 1968.

[24] M. Soumekh, "Bistatic synthetic aperture radar inversion with application in dynamic object imaging," *IEEE Trans. Signal Process.*, vol. 39, no. 9, pp. 2044–2055, Sep. 1991.

[25] V. Va and R. W. Heath, Jr., "Performance analysis of beam sweeping in millimeter wave assuming noise and imperfect antenna patterns," in *Proc. IEEE 84th Veh. Technol. Conf. (VTC-Fall)*, Sep. 2016, pp. 1–5.

[26] B. Sankur, "Statistical evaluation of image quality measures," *J. Electron. Imag.*, vol. 11, no. 2, p. 206, Apr. 2002.

[27] Z. Wang, A. C. Bovik, H. R. Sheikh, and E. P. Simoncelli, "Image quality assessment: From error visibility to structural similarity," *IEEE Trans. Image Process.*, vol. 13, no. 4, pp. 600–612, Apr. 2004.

Authors' photographs and biographies not available at the time of publication.